POLITECNICO DI TORINO
Repository ISTITUZIONALE

Purcell swimmer near a wall

Original
Purcell swimmer near a wall / Micalizio, E., Morandotti, M., Shum, H., Zoppello, M.. - In: MECCANICA. - ISSN 1572-9648. - 61:3(2026), pp. 1-16. [10.1007/s11012-026-02136-0]

Availability:
This version is available at: 11583/3011334 since: 2026-05-24T15:57:01Z

Publisher:
Springer

Published
DOI:10.1007/s11012-026-02136-0

Terms of use:

This article is made available under terms and conditions as specified in the corresponding bibliographic description in the repository

Publisher copyright

(Article begins on next page)

25 November 2026

RESEARCH

Purcell swimmer near a wall

Enrico Micalizio[1] · Marco Morandotti[1] · Henry Shum[2] · Marta Zoppello[1]

Received: 26 February 2026 / Revised: 22 April 2026 / Accepted: 10 May 2026
© The Author(s) 2026

Abstract
We study the effects of hydrodynamic interactions between a wall and a Purcell three-link swimmer in the case of motion in a plane. We extend previous theoretical studies of the three-link swimmer based on resistive-force theory by taking into account drag coefficients that are modified by the presence of a no-slip wall, considering the case where the distance to the wall is much less than the length of the swimmer and much larger than the thickness of the links. After deriving the equations of motion, we show, by means of criteria from Geometric Control Theory, that the system is locally controllable at configurations that are nearly parallel to the wall. Our result is obtained for a three-link swimmer in which the outer links have equal length and the central one differs by a factor $\lambda > 0$: controllability is achieved for all values of λ. For initially horizontal swimmers, the analytical displacements obtained from Lie brackets agree with the ones computed numerically with corresponding control gaits; moreover, we find values of λ that maximize the horizontal components of displacement. Numerical calculations are used to assess the effects of an approximation to the wall-induced drag correction used in the controllability proof. Furthermore, we numerically study first- and second-order controls applied to swimmers that are slightly tilted with respect to the wall and determine which components of net displacement depend on the orientation of the swimmer relative to the wall.

Keywords Microswimmers · Controllability · Resistive force Theory · Wall effects

1 Introduction

Low-Reynolds-number locomotion has been the subject of sustained interest since Purcell's seminal work on life at low Reynolds numbers [1]. In this regime, which is applicable to microorganisms and biomimetic microrobots, inertia is negligible and the motion of a swimmer results from non-reciprocal shape changes interacting with viscous forces. Among the paradigmatic models introduced by Purcell, the three-link swimmer now commonly referred to as the Purcell swimmer has become a key model for the theoretical study of microswimming [1], serving as a minimal yet rich system for the analysis of controllability, motion planning, and geometric aspects of locomotion.

In an unbounded planar fluid, the controllability properties of the Purcell swimmer are now well understood [2–5]. Modeling the swimmer as a kinematic control system driven by internal shape variables, several authors have shown that it is locally controllable around straight or moderately bent configurations [6, 7]. These results rely on Lie algebraic techniques and exploit the structure induced by the Stokes equations, which yield a driftless system with control vector fields associated with joint actuation. We note that these controllability results have been proved only for specific ratios λ of the length λL of the central link to the length L of the outer ones ($\lambda = 2$ in [3], $\lambda = 1$ in [4]).

Enrico Micalizio, Marco Morandotti, Henry Shum and Marta Zoppello have contributed equally to this work.

Published online: 22 May 2026

By contrast, the effect of boundaries on controllability has received comparatively less attention, despite its clear physical relevance. In realistic environments, microswimmers often operate in confined or partially bounded domains, where nearby walls modify hydrodynamic interactions through no-slip boundary conditions. From a control-theoretic viewpoint, the presence of a wall could alter the resistance matrix and breaks some of the symmetries present in the unbounded case. This naturally raises the question of whether such a boundary hinders controllability by restricting the accessible motions, or whether it may instead enrich the swimmer's dynamics and potentially enhance maneuverability.

It is commonly observed, for instance, that bacteria and spermatozoa tend to accumulate at surfaces and swim in circles near the surface [8–11]. Under steady propulsion, the symmetry-breaking of the wall induces a curved path, leading to the circular trajectory and, hence, confines the swimmer to a bounded region. Numerical and theoretical studies of swimming microorganisms have incorporated the effects of no-slip walls using image systems [12–14].

Motivated by the observation that many microorganisms use slender appendages for propulsion, the frameworks of resistive-force theory [15] and slender-body theory [16, 17] have been developed. In slender-body theory, a line distribution of Stokes flow singularities are placed along the centerline of the thin object with singularity strengths determined such that the appropriate fluid velocity boundary conditions are approximately matched on the surface of the object. By considering image singularities, the hydrodynamic effects of a no-slip wall can be incorporated [18]. In the resistive-force theory approach, a slender body is treated as a curve along which each point has drag coefficients characterizing the linear relationship between the local translational and rotational velocities (relative to the background fluid) and the forces and torques per unit length acting on the body. The coefficients are obtained from slender-body analyses and can be used to provide an approximate treatment of the wall. Expressions for the drag coefficients in the near-wall and far-field limits have been shown to agree well with numerical calculations for filaments [19].

The first objective of this paper is to address the question of controllability for a Purcell swimmer near a single planar wall and confined to motions in the plane perpendicular to the wall. Focusing on a configuration in which the swimmer is aligned and parallel to the wall, we derive the associated equation of motion using resistive-force theory with wall-induced hydrodynamic corrections [10, 18], casting it as a control system. We refer the reader to [19–23] for a list of references that take into account this wall-induced hydrodynamic correction of the drag coefficients.

Our main theoretical result (Theorem 1) shows that the presence of the wall is not an obstruction to controllability: the swimmer remains locally controllable near this aligned configuration. This demonstrates that, at least in this regime, confinement does not destroy the swimmer's ability to generate arbitrary small motions. We stress that our controllability result is obtained for all positive values of the length ratio λ.

Beyond the analysis of controllability via Lie bracket approximations, we investigate the net displacement generated by a classical small-amplitude Purcell stroke and by a corresponding second-order stroke when the swimmer starts from a straight configuration tilted with respect to the wall. By explicitly computing the induced motion, we show that the stroke produces a systematic drift in the direction of the initial orientation, without generating any net rotation. We further establish that the presence of the wall affects the norm of the displacement which is no longer constant as in an unbounded fluid domain; this norm is maximized when the swimmer is parallel to the wall.

This behavior differs from that reported in numerical simulations and experiments on swimming spermatozoa and bacteria, where more detailed descriptions of swimming gaits and hydrodynamic interactions typically predict a reorientation and progressive alignment with the wall, often leading to surface accumulation [8, 9, 11] or, in some regimes, escape [12, 24]. Although the forward-swimming gait for the Purcell swimmer is not hydrodynamically deflected by the wall as it approaches, we show with results from a control-oriented framework based on Lie bracket computations that the swimmer can be steered both toward and away from the wall by adjusting its gait.

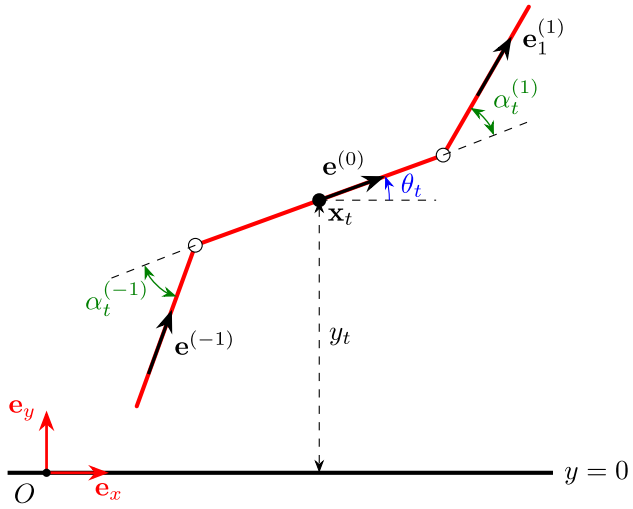


Fig. 1 Representation of the Purcell swimmer near the wall

2 Mathematical model

We consider a system composed of a three-link swimmer and a rigid wall, modeled as a straight line in our 2D model, and we adopt a reference frame in which the wall coincides with the x-axis. Let us denote by y_t the distance, at time t, between the wall and the midpoint of the central link, whose position in the plane, at time t, is $\mathbf{x}_t = (x_t, y_t)$. Moreover, the orientation of the central link with respect to the wall is described by the angle $\theta_t \in [-\pi, \pi)$, while the relative angles between the central link and the two outer links are denoted by $\alpha_t^{(\pm 1)} \in [-\pi, \pi)$, see Fig. 1.

Thus, the triple (x_t, y_t, θ_t) describes the global position of the swimmer at time t, whereas the pair $\boldsymbol{\alpha}_t := \left[\alpha_t^{(-1)}, \alpha_t^{(1)}\right]^\top$ represents the shape. Each link has constant length L_i ($i \in \{\pm 1, 0\}$) and thickness r, and we assume that

$$0 < r \ll L_i \quad \text{for every } i \in \{\pm 1, 0\}. \tag{1}$$

We also assume that all parts of the swimmer are far from the wall compared with r,

$$y_t \pm \frac{L_0}{2} \sin\theta_t \gg r, \quad \text{for every } t \text{ and} \tag{2a}$$

$$y_t + i\left(\frac{L_0}{2} \sin\theta_t + L_i \sin(\theta_t + \alpha_t^{(i)})\right) \gg r, \quad \text{for } i = \pm 1 \text{ and for every } t. \tag{2b}$$

We denote by $\mathbf{e}_t^{(i)}$ the unit vector describing the direction of the i-th link, defined as

$$\mathbf{e}_t^{(i)} := \begin{bmatrix} \cos\left(\theta_t + i^2 \alpha_t^{(i)}\right) \\ \sin\left(\theta_t + i^2 \alpha_t^{(i)}\right) \end{bmatrix}, \qquad \text{for } i = -1, 0, 1$$

(we can fictitiously define $\alpha_t^{(0)} = 0$; its contribution is irrelevant). Finally, we can express the position of a point $\mathbf{x}_t^{(i)}(s)$ on the i-th link

$$\mathbf{x}_t^{(i)}(s) = \mathbf{x}_t + \sigma_-^{(i)} \frac{L_0}{2} \mathbf{e}_t^{(0)} + \sigma_+^{(i)} s\, \mathbf{e}_t^{(i)}, \tag{3}$$

where $s \in [0, L_i]$ denotes the distance along the i-th link from its hinge, and where we have defined $\sigma_{\pm}^{(i)} := \text{sign}(i \pm \frac{1}{2})$.[1] Taking the time derivative in (3), the velocity of the generic point in the three-link swimmer reads

$$\dot{\mathbf{x}}_t^{(i)}(s) = \dot{\mathbf{x}}_t + \sigma_-^{(i)} \frac{L_0}{2} \dot{\theta}_t \, \mathbf{n}_t^{(0)} + \sigma_+^{(i)} s \left(\dot{\theta}_t + i^2 \dot{\alpha}_t^{(i)}\right) \mathbf{n}_t^{(i)}, \tag{4}$$

where $\mathbf{n}_t^{(i)} := R_{\pi/2} \mathbf{e}_t^{(i)}$ is the normal vector obtained by rotating the tangent vector $\mathbf{e}_t^{(i)}$ by $\pi/2$.

Now, we aim to apply Resistive Force Theory [15] to compute the hydrodynamic force and torque densities acting on the swimmer. However, in the presence of a wall, the drag coefficients (usually denoted by $C_\parallel$ and $C_\perp$ when they are constant) depend explicitly on the distance $d_t^{(i)}(s) = y_t^{(i)}(s)$ of the point $\mathbf{x}_t^{(i)}(s)$ from the wall. Of particular interest is the near-wall case in which

$$y_t \ll L_i \,, \quad \text{for every } i \in \{\pm 1, 0\} \text{ and for every } t. \tag{5}$$

as the wall would have a more significant effect. By considering line integrals of Stokeslets and their image systems, Katz *et al.* [18, equation (2.7)] derived the drag coefficients for a thin cylinder parallel to a no-slip wall for motions in the directions perpendicular to the wall and parallel to the axis of the cylinder (see also [25, Section 2.7] and [19, equation (2.35)]),

$$C_\perp = \frac{4\pi\mu}{\log\left(2d/r\right) - 1} \qquad \text{and} \qquad C_\parallel = \frac{2\pi\mu}{\log\left(2d/r\right)},$$

where $\mu > 0$ is the dynamic viscosity, under the assumption that the distance d to the wall is much greater than the thickness r of the cylinder and much smaller than the length of the cylinder. In the regime $2d/r \gg 1$, we can assume that $C_\perp = 2C_\parallel$. We use these coefficients to define the local force and torque densities along the links of the Purcell swimmer. Taking into account the variations in distance to the wall along each link, we have

$$C_{\perp t}^{(i)}(s) = \frac{4\pi\mu}{\log\left(2d_t^{(i)}(s)/r\right)} = 2C_{\parallel t}^{(i)}(s), \tag{6}$$

Consistent with the derivation of the drag coefficients [18], we impose the constraints $d_t^{(i)}(s) = y_t^{(i)}(s) \gg r$, recall (1).

In the sequel, we will omit the explicit dependence of the drag coefficients from t. Let $\mathbf{f}_t^{(i)}(s)$ be the hydrodynamic force density acting on the point $\mathbf{x}_t^{(i)}(s)$ of the i-th link. Resistive Force Theory yields

$$\begin{aligned}
\mathbf{f}_t^{(i)}(s) &= \left[(C_\parallel^{(i)}(s) - C_\perp^{(i)}(s))\mathbf{e}_t^{(i)} \otimes \mathbf{e}_t^{(i)} + C_\perp^{(i)}(s)\mathbf{I}_2\right]\dot{\mathbf{x}}_t^{(i)}(s) \\
&= C_\perp^{(i)}(s)\Bigg[\left(\mathbf{I}_2 - \frac{1}{2}\mathbf{E}_t^{(i)}\right)\dot{\mathbf{x}}_t + \sigma_+^{(i)} s\left(\dot{\theta}_t + i^2\dot{\alpha}_t^{(i)}\right)\mathbf{n}_t^{(i)} \\
&\quad + \sigma_-^{(i)} \frac{L_0}{2}\dot{\theta}_t\left(\mathbf{I}_2 - \frac{1}{2}\mathbf{E}_t^{(i)}\right)\mathbf{n}_t^{(0)}\Bigg],
\end{aligned} \tag{7}$$

[1] The explicit values of $\sigma_{\pm}^{(i)}$ are $\sigma_-^{(-1)} = \sigma_-^{(0)} = \sigma_+^{(-1)} = -1$ and $\sigma_-^{(1)} = \sigma_+^{(0)} = \sigma_+^{(1)} = 1$.

where we defined $\mathbf{E}_t^{(i)} := \mathbf{e}_t^{(i)} \otimes \mathbf{e}_t^{(i)}$ for notational convenience, and $\mathbf{I}_2$ is the 2×2 identity matrix. Using (7) and defining $\sigma_*^{(i)} := \text{sign}(i^2 - \frac{1}{2})$,[2] the torque density about the reference point $\mathbf{x}_t$ is given by

$$\begin{aligned}\tau_t^{(i)}(s) = C_\perp^{(i)}(s)\Big[&\sigma_-^{(i)}\frac{L_0}{2}\mathbf{n}_t^{(0)}\cdot\left(\mathbf{I}_2-\frac{1}{2}\mathbf{E}_t^{(i)}\right)\dot{\mathbf{x}}_t+\sigma_+^{(i)}s\,\mathbf{n}_t^{(i)}\cdot\left(\mathbf{I}_2-\frac{1}{2}\mathbf{E}_t^{(i)}\right)\dot{\mathbf{x}}_t\\&+\frac{L_0^2}{4}\dot{\theta}_t\mathbf{n}_t^{(0)}\cdot\left(\mathbf{I}_2-\frac{1}{2}\mathbf{E}_t^{(i)}\right)\mathbf{n}_t^{(0)}+\sigma_*^{(i)}\frac{L_0}{2}\dot{\theta}_t s\,\mathbf{n}_t^{(i)}\cdot\left(\mathbf{I}_2-\frac{1}{2}\mathbf{E}_t^{(i)}\right)\mathbf{n}_t^{(0)}\\&+\sigma_*^{(i)}\frac{L_0}{2}s\left(\dot{\theta}_t+i^2\dot{\alpha}_t^{(i)}\right)\mathbf{n}_t^{(0)}\cdot\mathbf{n}_t^{(i)}+s^2\left(\dot{\theta}_t+i^2\dot{\alpha}_t^{(i)}\right)\Big].\end{aligned} \tag{8}$$

Therefore, the total force and torque acting on each link are given by integrating (7) and (8), respectively, over $s \in [0, L_i]$, and adding up all the contributions for $i = -1, 0, 1$. Yet, since the expressions in (7) and (8) do not admit closed-form expressions when integrated with respect to s, we proceed by using a second-order Taylor approximation of the coefficients. This is done using the approximation $d_t^{(i)}(s) \simeq y_t$, which is valid when the swimmer is nearly parallel to the wall so that the difference between the closest and furthest distances on any point on the swimmer to the wall is small compared with y_t.

We obtain the following expression, up to second order in s

$$C_\perp^{(i)}(s) \simeq G_t^{(i)} + sH_t^{(i)} + s^2K_t^{(i)}, \tag{9a}$$

where we have defined

$$G_t^{(i)} := \frac{2\pi\mu}{\ell_t}\left[2-\frac{\sigma_-^{(i)}L_0\sin(\theta_t)}{y_t\ell_t}+\frac{L_0^2}{4}\frac{\sin^2(\theta_t)}{y_t\ell_t^2}\left(1+\frac{2}{\ell_t}\right)\right], \tag{9b}$$

$$H_t^{(i)} := -\frac{2\pi\mu\sin\left(\theta_t+i^2\alpha_t^{(i)}\right)}{y_t\ell_t^2}\left[2\sigma_+^{(i)}-\frac{\sigma_*^{(i)}\,L_0\sin(\theta_t)}{y_t}\left(1+\frac{2}{\ell_t}\right)\right], \tag{9c}$$

$$K_t^{(i)} := \frac{2\pi\mu\sigma_+^{(i)}\sin^2\left(\theta_t+i^2\alpha_t^{(i)}\right)}{y_t^2\ell_t^2}\left(1+\frac{2}{\ell_t}\right), \tag{9d}$$

with $\ell_t := \log(2y_t/r)$. Thanks to (9), we can integrate (7) and (8) with respect to $s \in [0, L_i]$ (for $i = \pm1, 0$) and obtain analytic expressions. The resulting total force and torque exerted by the fluid on the swimmer are then given by

$$\mathbf{F}_t = \sum_{i=-1}^{1}\int_0^{L_i}\mathbf{f}_t^{(i)}(s)\,\mathrm{d}s = \mathbf{A}_t\dot{\mathbf{x}}_t + \mathbf{B}_t\dot{\boldsymbol{\alpha}}_t + \boldsymbol{\gamma}_t\dot{\theta}_t, \tag{10a}$$

$$T_t = \sum_{i=-1}^{1}\int_0^{L_i}\tau_t^{(i)}(s)\,\mathrm{d}s = \boldsymbol{\gamma}_t\cdot\dot{\mathbf{x}}_t + \mathbf{b}_t\cdot\dot{\boldsymbol{\alpha}}_t + \delta_t\dot{\theta}_t. \tag{10b}$$

In (10), we have defined the 2×2 matrices $\mathbf{A}_t$ and $\mathbf{B}_t$ by

$$\mathbf{A}_t := \sum_{i=-1}^{1}\left(G_t^{(i)}L_i + H_t{}^{(i)}\frac{L_i^2}{2} + K_t^{(i)}\frac{L_i^3}{3}\right)\left(\mathbf{I}_2-\frac{1}{2}\mathbf{E}_t^{(i)}\right),$$

[2] The explicit values of $\sigma_*^{(i)}$ are $\sigma_*^{(\pm1)} = 1$ and $\sigma_*^{(0)} = -1$. Notice that $\sigma_*^{(i)} = \sigma_-^{(i)}\sigma_+^{(i)}$.

 https://doi.org/10.1007/s11012-026-02136-0

$$\mathbf{B}_t := \Bigg[-\left(G_t^{(-1)}\frac{L_{-1}^2}{2} + {H_t}^{(-1)}\frac{L_{-1}^3}{3} + K_t^{(-1)}\frac{L_{-1}^4}{4}\right)\mathbf{n}_t^{(-1)} \Bigg| \left(G_t^{(1)}\frac{L_1^2}{2} + {H_t}^{(1)}\frac{L_1^3}{3} + K_t^{(1)}\frac{L_1^4}{4}\right)\mathbf{n}_t^{(1)} \Bigg]$$

(notice that $\mathbf{A}_t$ is symmetric), the vectors $\boldsymbol{\gamma}_t$ and $\mathbf{b}_t$ by

$$\begin{aligned}
\boldsymbol{\gamma}_t &:= \sum_{i=-1}^{1} \Bigg[\left(G_t^{(i)}\frac{L_i^2}{2} + {H_t}^{(i)}\frac{L_i^3}{3} + K_t^{(i)}\frac{L_i^4}{4}\right)\sigma_+^{(i)}\mathbf{n}_t^{(i)} \\
&\quad + \frac{L_0}{2}\sigma_-^{(i)}\left(G_t^{(i)}L_i + {H_t}^{(i)}\frac{L_i^3}{3} + K_t^{(i)}\frac{L_i^4}{4}\right)\left(\mathbf{I}_2 - \frac{1}{2}\mathbf{E}_t^{(i)}\right)\mathbf{n}_t^{(0)} \Bigg], \\
\mathbf{b}_t &:= \Bigg[\frac{L_0}{2}\left(G_t^{(-1)}\frac{L_{-1}^2}{2} + {H_t}^{(-1)}\frac{L_{-1}^3}{3} + K_t^{(-1)}\frac{L_{-1}^4}{4}\right)\mathbf{n}_t^{(0)}\cdot\mathbf{n}_t^{(-1)} \\
&\quad + \left(G_t^{(-1)}\frac{L_{-1}^3}{3} + {H_t}^{(-1)}\frac{L_{-1}^4}{4} + K_t^{(-1)}\frac{L_{-1}^5}{5}\right) \Bigg| \\
&\quad \frac{L_0}{2}\left(G_t^{(1)}\frac{L_1^2}{2} + {H_t}^{(1)}\frac{L_1^3}{3} + K_t^{(1)}\frac{L_1^4}{4}\right)\mathbf{n}_t^{(0)}\cdot\mathbf{n}_t^{(1)} + \left(G_t^{(1)}\frac{L_1^3}{3} + {H_t}^{(1)}\frac{L_1^4}{4} + K_t^{(1)}\frac{L_1^5}{5}\right) \Bigg],
\end{aligned}$$

and the scalar δ_t by

$$\begin{aligned}
\delta_t := \sum_{i=-1}^{1} \Bigg[& \frac{L_0^2}{4}\left(G_t^{(i)}L_i + {H_t}^{(i)}\frac{L_i^2}{2} + K_t^{(i)}\frac{L_i^3}{3}\right)\mathbf{n}_t^{(0)}\cdot\left(\mathbf{I}_2 - \frac{1}{2}\mathbf{E}_t^{(i)}\right)\mathbf{n}_t^{(0)} \\
& + \frac{L_0}{2}\sigma_*^{(i)}\left(G_t^{(i)}\frac{L_i^2}{2} + {H_t}^{(i)}\frac{L_i^3}{3} + K_t^{(i)}\frac{L_i^4}{4}\right)\mathbf{n}_t^{(0)}\cdot\left(2\mathbf{I}_2 - \frac{1}{2}\mathbf{E}_t^{(i)}\right)\mathbf{n}_t^{(0)} \\
& + G_t^{(i)}\frac{L_i^3}{3} + {H_t}^{(i)}\frac{L_i^4}{4} + K_t^{(i)}\frac{L_i^5}{5} \Bigg].
\end{aligned}$$

Finally, from (10), the equations of motion can be written compactly as

$$\mathbf{0} = \begin{bmatrix}\mathbf{F}_t \\ T_t\end{bmatrix} = \begin{bmatrix}\mathbf{A}_t & \boldsymbol{\gamma}_t & \mathbf{B}_t \\ \boldsymbol{\gamma}_t^\top & \delta_t & \mathbf{b}_t^\top\end{bmatrix}\begin{bmatrix}\dot{\mathbf{x}}_t \\ \dot{\theta}_t \\ \dot{\boldsymbol{\alpha}}_t\end{bmatrix} = \begin{bmatrix}(\mathbf{A}_t)_{11} & (\mathbf{A}_t)_{12} & (\boldsymbol{\gamma}_t)_1 & (\mathbf{B}_t)_{11} & (\mathbf{B}_t)_{12} \\ (\mathbf{A}_t)_{21} & (\mathbf{A}_t)_{22} & (\boldsymbol{\gamma}_t)_2 & (\mathbf{B}_t)_{21} & (\mathbf{B}_t)_{22} \\ (\boldsymbol{\gamma}_t)_1 & (\boldsymbol{\gamma}_t)_2 & \delta_t & (\mathbf{b}_t)_1 & (\mathbf{b}_t)_2\end{bmatrix}\begin{bmatrix}\dot{x}_t \\ \dot{y}_t \\ \dot{\theta}_t \\ \dot{\alpha}_t^{(-1)} \\ \dot{\alpha}_t^{(1)}\end{bmatrix}. \tag{11}$$

3 Controllability

To study the controllability of the system, we employ tools from Geometric Control Theory. Starting from equation (11), we introduce two control functions $t \mapsto u_t^{(\pm 1)}$ corresponding to the shape changes governed by $\dot{\alpha}_t^{(\pm 1)}$, respectively. Eventually, we will define the associated control fields $\mathbf{h}_t^{(\pm 1)}$ which will be used to compute Lie brackets and analyze the controllability of the system.

By introducing

$$\mathbf{M}_t := \begin{bmatrix} \mathbf{A}_t & \boldsymbol{\gamma}_t \\ \boldsymbol{\gamma}_t^\top & \delta_t \end{bmatrix}, \quad \mathbf{g}_t^{(-1)} := \begin{bmatrix} (\mathbf{B}_t)_{11} \\ (\mathbf{B}_t)_{21} \\ (\mathbf{b}_t)_1 \end{bmatrix}, \quad \text{and} \quad \mathbf{g}_t^{(1)} := \begin{bmatrix} (\mathbf{B}_t)_{12} \\ (\mathbf{B}_t)_{22} \\ (\mathbf{b}_t)_2 \end{bmatrix},$$

and the control inputs $[u_t^{(-1)}, u_t^{(1)}]^\top := [\dot{\alpha}_t^{(-1)}, \dot{\alpha}_t^{(1)}]^\top$, the equations of motion (11) can be rewritten as

$$\begin{bmatrix} \mathbf{M}_t & \mathbf{0}_{3\times 2} \\ \mathbf{0}_{2\times 3} & \mathbf{I}_2 \end{bmatrix} \begin{bmatrix} \dot{\mathbf{x}}_t \\ \dot{\theta}_t \\ \dot{\boldsymbol{\alpha}}_t \end{bmatrix} = - \begin{bmatrix} \mathbf{g}_t^{(-1)} & \mathbf{g}_t^{(1)} \\ 1 & 0 \\ 0 & 1 \end{bmatrix} \begin{bmatrix} u_t^{(-1)} \\ u_t^{(1)} \end{bmatrix}. \tag{12}$$

The matrix $\mathbf{M}_t$ is usually referred to as the *grand resistance matrix*; it is symmetric and invertible around the "flat" ($\alpha_t^{(\pm 1)} = 0$) horizontal ($\theta_t = 0$) configuration, at which we have $\det \mathbf{M}_t = 8\pi^3\mu^3(L_{-1} + L_0 + L_1)^5/3\ell_t^3 \neq 0$. By continuity of the determinant with respect to the matrix entries, $\det \mathbf{M}_t$ remains different from zero also at configurations $\theta_t, \alpha_t^{(\pm 1)} \approx 0$. This allows us to solve (12) for the position and shape variables and write it as a nonlinear driftless affine control system

$$\begin{bmatrix} \dot{\mathbf{x}}_t \\ \dot{\theta}_t \\ \dot{\boldsymbol{\alpha}}_t \end{bmatrix} = \mathbf{h}_t^{(-1)} u_t^{(-1)} + \mathbf{h}_t^{(1)} u_t^{(1)} \tag{13}$$

where the control vector fields $\mathbf{h}_t^{(\pm 1)}$ are defined by

$$\mathbf{h}_t^{(-1)} := \begin{bmatrix} -\mathbf{M}_t^{-1}\mathbf{g}_t^{(-1)} \\ 1 \\ 0 \end{bmatrix}, \qquad \mathbf{h}_t^{(1)} := \begin{bmatrix} -\mathbf{M}_t^{-1}\mathbf{g}_t^{(1)} \\ 0 \\ 1 \end{bmatrix}.$$

We are now ready to investigate the local controllability of (13). To simplify computations, we suppose that the outer links have length $L_{-1} = L_1 = L$ and that the central one has length $L_0 = \lambda L$, for some $\lambda > 0$, provided that (1) and (2) are respected.

Theorem 1 *Let $L, r, \lambda > 0$ and let $L_{\pm 1} = L$, $L_0 = \lambda L$; let us assume that (1) and (2) hold true. Then control system (13) is locally controllable around an aligned configuration parallel to the wall, i.e., for $\theta_t, \alpha_t^{(\pm 1)} \approx 0$.*

Proof In order to prove the local controllability of the system (13) we resort to the Chow–Rashewskii theorem [26, Theorem 5.9], which states that a sufficient condition for local controllability at a certain configuration is that the Lie algebra generated by the control vector fields at that configuration has dimension equal to the dimension of the tangent space of the overall system. In our specific case, we have to show that the control vector fields $\mathbf{h}_t^{(\pm 1)}$ and their iterated Lie brackets at $(x_t, y_t, \theta_t, \alpha_t^{(-1)}, \alpha_t^{(1)}) = (x_t, y_t, 0, 0, 0) =: \mathbf{s}_t^0$ generate a space of dimension five. Through explicit computations, we obtain

$$\mathbf{h}_t^1(\lambda) := \mathbf{h}_t^{(-1)}\big|_{\mathbf{s}_t^0} = \begin{bmatrix} 0 \\ \dfrac{L}{2\lambda + 4} \\ \dfrac{-3\lambda - 4}{(\lambda + 2)^3} \\ 1 \\ 0 \end{bmatrix}, \qquad \mathbf{h}_t^2(\lambda) := \mathbf{h}_t^{(1)}\big|_{\mathbf{s}_t^0} = \begin{bmatrix} 0 \\ -\dfrac{L}{2\lambda + 4} \\ \dfrac{-3\lambda - 4}{(\lambda + 2)^3} \\ 0 \\ 1 \end{bmatrix},$$

 https://doi.org/10.1007/s11012-026-02136-0

$$\mathbf{h}_t^3(\lambda) := [\mathbf{h}_t^{(-1)}, \mathbf{h}_t^{(1)}]\big|_{\mathbf{s}_t^0} = \begin{bmatrix} \frac{L\lambda(2\lambda+3)}{(\lambda+2)^4} \\ 0 \\ 0 \\ 0 \\ 0 \end{bmatrix}, \tag{14}$$

$$\mathbf{h}_t^4(\lambda) := [\mathbf{h}_t^{(1)}, [\mathbf{h}_t^{(-1)}, \mathbf{h}_t^{(1)}]]\big|_{\mathbf{s}_t^0} = \begin{bmatrix} -\frac{L^2\lambda(4\lambda^4+7\lambda^3-18\lambda^2-52\lambda-34)}{6(\lambda+2)^7\ell_t y_t} \\ \frac{L\lambda^2(3\lambda^3+20\lambda^2+38\lambda+22)}{2(\lambda+2)^7} \\ \frac{3\lambda}{(\lambda+2)^4} \\ 0 \\ 0 \end{bmatrix}, \tag{15}$$

$$\mathbf{h}_t^5(\lambda) := [\mathbf{h}_t^{(-1)}, [\mathbf{h}_t^{(-1)}, \mathbf{h}_t^{(1)}]]\big|_{\mathbf{s}_t^0} = \begin{bmatrix} \frac{L^2\lambda(4\lambda^4+7\lambda^3-18\lambda^2-52\lambda-34)}{6(\lambda+2)^7\ell_t y_t} \\ \frac{L\lambda^2(3\lambda^3+20\lambda^2+38\lambda+22)}{2(\lambda+2)^7} \\ -\frac{3\lambda}{(\lambda+2)^4} \\ 0 \\ 0 \end{bmatrix}.$$

Finally, we can compute the determinant of the resulting 5×5 matrix, which reads

$$D(\lambda) := \det\big(\mathbf{h}_t^1(\lambda) \,|\, \mathbf{h}_t^2(\lambda) \,|\, \mathbf{h}_t^3(\lambda) \,|\, \mathbf{h}_t^4(\lambda) \,|\, \mathbf{h}_t^5(\lambda)\big) = -\frac{3L^2\lambda^4(2\lambda+3)(3\lambda^3+20\lambda^2+38\lambda+22)}{(\lambda+2)^{15}},$$

which is negative for every $\lambda > 0$.

This proves the local controllability of the system at the configuration $\mathbf{s}_t^0$ for every $\lambda > 0$.

For tilted configurations at which $\theta_0 \neq 0$ is sufficiently small in magnitude, the system remains locally controllable. Indeed, since the vector fields and their Lie brackets are real analytic, their determinant is a continuous function. Therefore, the determinant in the configuration $(x_0, y_0, \theta_0, 0, 0)$ will remain different from zero, proving local controllability. □

Remark 1 It is well known (see, e.g., [27]) that the displacement of the system which starts in the aligned configuration parallel to the wall after a periodic control stroke with piecewise constant controls is given by a multiple of the first order bracket $\mathbf{h}_t^3(\lambda)$. From (14), it emerges that this results in a displacement parallel to the wall, independently from the distance of the swimmer from the wall, for all values of λ. Notice that this independence is not linked to the symmetric design of the three-link swimmer: indeed, if the three links all have different lengths, the Lie bracket at the aligned configuration parallel to the wall is given by

$$\mathbf{h}_t^3(L_{-1}, L_0, L_1) = \begin{bmatrix} \frac{L_0L_1L_{-1}\big(L_1(L_0+L_1)+(L_0+L_1)L_{-1}+L_{-1}^2\big)}{(L_0+L_1+L_{-1})^4} \\ 0 \\ 0 \\ 0 \\ 0 \end{bmatrix},$$

and notice that $\mathbf{h}_t^3(L, \lambda L, L) = \mathbf{h}_t^3(\lambda)$. Therefore, we can conclude that if the swimmer is parallel to the wall, after making a small periodic control stroke with piecewise controls, it will move parallel to the wall, regardless of the length of the links.

4 Numerical simulations

In this section, we take advantage of numerical tools to solve the control system (13). The approximation (9a) of the drag coefficients, which was a simplification that allowed analytical controllability results to be obtained, is not necessary for the numerical solutions. We begin with a sensitivity analysis to determine whether this approximation has a significant effect on the dynamics and then present additional characterizations of the system using the nonlinear coefficients (6), including the dependence of the spatial and angular displacements on the link length ratio λ introduced in Theorem 1.

We solve the control system (13) in MATLAB using the `ode45` function, which is an implementation of the Runge–Kutta–Fehlberg 4(5) numerical ODE solver. The controls $u_t^{(-1)}$ and $u_t^{(1)}$ are defined as piecewise constant functions with an amplitude parameter $\xi > 0$ such that the net displacement after one period of the control corresponds to the defined vector fields $\mathbf{h}_t^1, \ldots, \mathbf{h}_t^5$, respectively, in the limit of $\xi \to 0$.

For numerical simulations corresponding to the vector field $\mathbf{h}_t^3 = [\mathbf{h}_t^1, \mathbf{h}_t^2]$, which results in swimming along the direction of the links, we start from the straight configuration $\alpha_0^{(-1)} = \alpha_0^{(1)} = 0$ and apply the 4-periodic controls

$$u_t^{(-1)} = \begin{cases} \xi, & t \bmod 4 \in [0,1), \\ 0, & t \bmod 4 \in [1,2), \\ -\xi, & t \bmod 4 \in [2,3), \\ 0, & t \bmod 4 \in [3,4), \end{cases} \qquad u_t^{(1)} = \begin{cases} 0, & t \bmod 4 \in [0,1), \\ \xi, & t \bmod 4 \in [1,2), \\ 0, & t \bmod 4 \in [2,3), \\ -\xi, & t \bmod 4 \in [3,4). \end{cases} \tag{16}$$

The normalized displacements per cycle are given by (see, *e.g.*, [26, Section 1.4] or [27, Section 3.2])

$$\boldsymbol{\Delta} = \begin{bmatrix} \Delta x \\ \Delta y \\ \Delta\theta \\ \Delta\alpha^{(-1)} \\ \Delta\alpha^{(1)} \end{bmatrix} := \frac{1}{\xi^2} \begin{bmatrix} x_4 - x_0 \\ y_4 - y_0 \\ \theta_4 - \theta_0 \\ \alpha_4^{(-1)} - \alpha_0^{(-1)} \\ \alpha_4^{(1)} - \alpha_0^{(1)} \end{bmatrix} = \mathbf{h}_0^3 + \begin{bmatrix} O(\xi) \\ O(\xi) \\ O(\xi) \\ 0 \\ 0 \end{bmatrix} \tag{17}$$

as $\xi \to 0$. In Fig. 2, the x, y, and θ components of $\boldsymbol{\Delta}$ are plotted along with their corresponding components of $\mathbf{h}_t^3$ starting from a straight configuration of the links parallel to the wall. The numerical results converge to the asymptotic result as $\xi \to 0$. We note that for finite ξ there is a slight drift away from the wall ($\Delta y > 0$) when the swimmer is initially parallel to the wall. The magnitude of $\Delta\theta$ computed using the full drag coefficients is insignificant for all tested ξ. We note, however, that the error (compared with the asymtotic result) in $\Delta\theta$ computed with the full coefficient formula increases when ξ decreases below about $10^{-3.5}$. We attribute this to numerical errors resulting from imperfect cancellation of small displacements over the periodic cycle of motion.

To support our theoretical controllability result, we also numerically simulate controls corresponding to the second-order vector field $\mathbf{h}_t^4 = [\mathbf{h}_t^2, [\mathbf{h}_t^1, \mathbf{h}_t^2]]$, which results in swimming along the direction perpendicular to the links and a rotation of the swimmer. Starting from the straight configuration $\alpha_0^{(-1)} = \alpha_0^{(1)} = 0$, we apply the

 https://doi.org/10.1007/s11012-026-02136-0

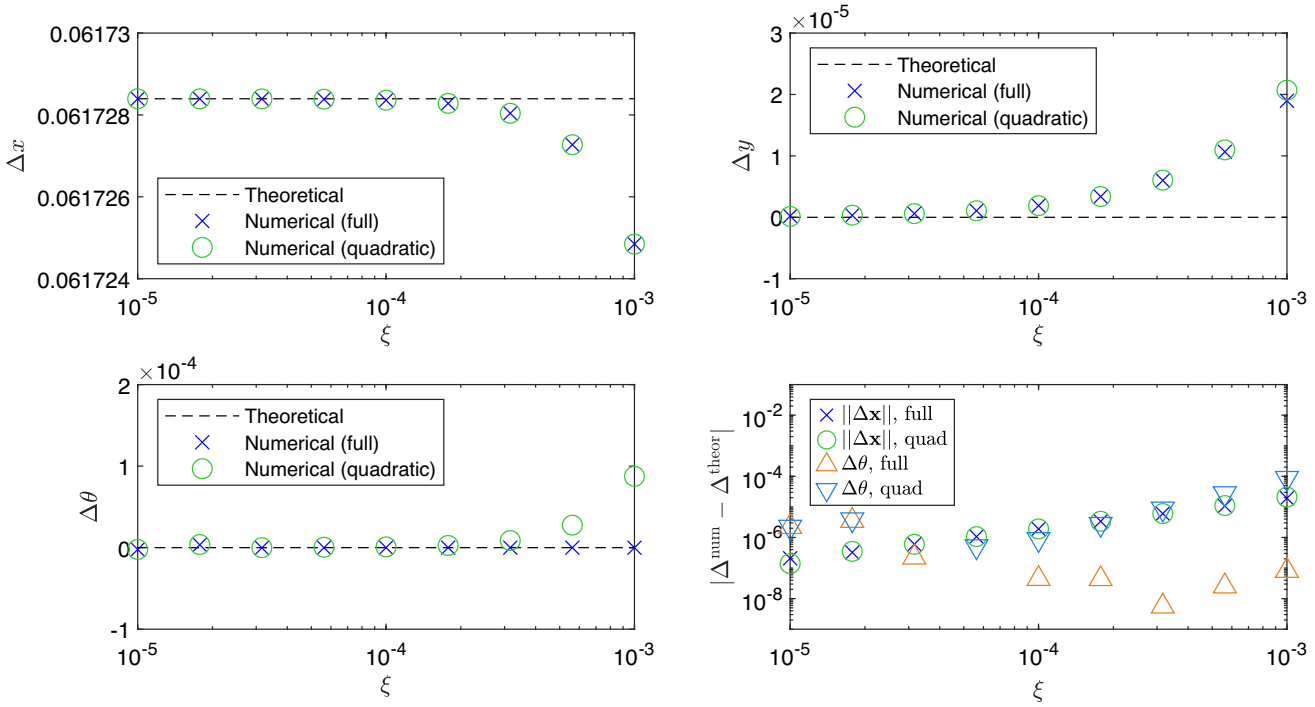


Fig. 2 Normalized displacements Δx, Δy, and $\Delta\theta$ for a swimming stroke corresponding to the vector field $\mathbf{h}_t^3$. The values computed numerically using the full drag coefficients (6) and the quadratic approximation (9) are compared as functions of stroke amplitude ξ, and the corresponding theoretical values for the limit $\xi \to 0$ from the vector field $\mathbf{h}_t^3$ are indicated. The initial state is $(x_0, y_0, \theta_0, \alpha_0^{(-1)}, \alpha_0^{(1)}) = (0, 10^{-2}, 0, 0, 0)$. The geometrical parameters used are $L = 1$, $\lambda = 1$, $r = 10^{-4}$. The theoretical values from $\mathbf{h}_t^3$ are $\Delta x \approx 0.0617$, $\Delta y = \Delta\theta = 0$. At $\xi = 10^{-4.25}$, we found $|\Delta\theta^{\text{num}} - \Delta\theta^{\text{theor}}| = 0$ for the full coefficients so this data point is not shown on the logarithmic scale

10-periodic controls

$$u_t^{(-1)} = \begin{cases} 0, & t \bmod 10 \in [0,1), \\ \xi, & t \bmod 10 \in [1,2), \\ 0, & t \bmod 10 \in [2,3), \\ -\xi, & t \bmod 10 \in [3,4), \\ 0, & t \bmod 10 \in [4,5), \\ 0, & t \bmod 10 \in [5,6), \\ 0, & t \bmod 10 \in [6,7), \\ \xi, & t \bmod 10 \in [7,8), \\ 0, & t \bmod 10 \in [8,9), \\ -\xi, & t \bmod 10 \in [9,10), \end{cases} \qquad u_t^{(1)} = \begin{cases} \xi, & t \bmod 10 \in [0,1), \\ 0, & t \bmod 10 \in [1,2), \\ \xi, & t \bmod 10 \in [2,3), \\ 0, & t \bmod 10 \in [3,4), \\ -\xi, & t \bmod 10 \in [4,5), \\ -\xi, & t \bmod 10 \in [5,6), \\ \xi, & t \bmod 10 \in [6,7), \\ 0, & t \bmod 10 \in [7,8), \\ -\xi, & t \bmod 10 \in [8,9), \\ 0, & t \bmod 10 \in [9,10). \end{cases} \tag{18}$$

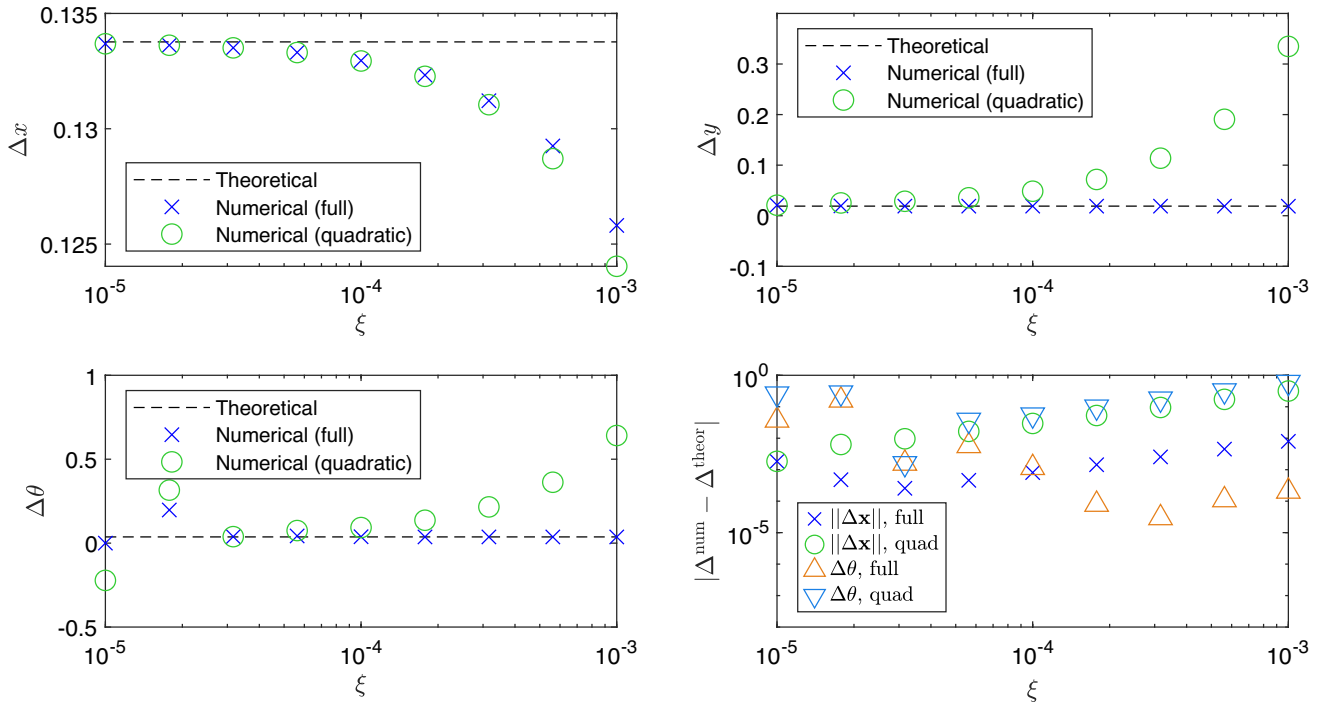


Fig. 3 Normalized displacements Δx, Δy, and $\Delta\theta$ for a swimming stroke corresponding to the vector field $\mathbf{h}_t^4$. The values computed numerically using the full drag coefficients (6) and the quadratic approximation (9) are compared as functions of stroke amplitude ξ, and the corresponding theoretical values for the limit $\xi \to 0$ from the vector field $\mathbf{h}_t^4$ are indicated. The initial state is $(x_0, y_0, \theta_0, \alpha_0^{(-1)}, \alpha_0^{(1)}) = (0, 10^{-2}, 0, 0, 0)$. The geometrical parameters used are $L = 1$, $\lambda = 1$, $r = 10^{-4}$. The theoretical values from $\mathbf{h}_t^4$ are $(\Delta x, \Delta y, \Delta\theta) \approx (0.1338, 0.0190, 0.0370)$

We define the normalized displacements per cycle for this family of controls by

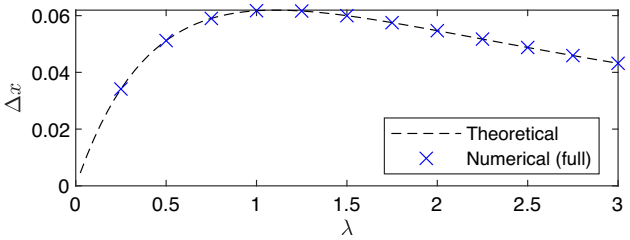
$$\boldsymbol{\Delta} = \begin{bmatrix} \Delta x \\ \Delta y \\ \Delta\theta \\ \Delta\alpha^{(-1)} \\ \Delta\alpha^{(1)} \end{bmatrix} := \frac{1}{\xi^3} \begin{bmatrix} x_{10} - x_0 \\ y_{10} - y_0 \\ \theta_{10} - \theta_0 \\ \alpha_{10}^{(-1)} - \alpha_0^{(-1)} \\ \alpha_{10}^{(1)} - \alpha_0^{(1)} \end{bmatrix} = \mathbf{h}_0^4 + \begin{bmatrix} O(\xi) \\ O(\xi) \\ O(\xi) \\ 0 \\ 0 \end{bmatrix} \tag{19}$$

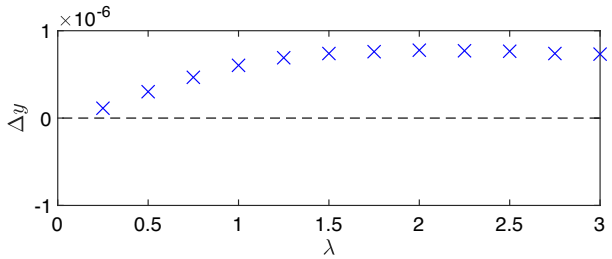
as $\xi \to 0$. Numerically evaluated normalized displacements are shown in Fig. 3. Discrepancies between the finite-ξ computations and the theoretical asymptotic limit are generally larger than those found for the $\mathbf{h}_t^3$ vector field. Since the second-order control yields a much smaller $O(\xi^3)$ net displacement before normalization, computations are more susceptible to round-off and other numerical errors.

Note that $\mathbf{h}_t^5$ has the same components, possibly up to a sign, of $\mathbf{h}_t^4$, so we do not present numerical results for it. The comparisons done so far and presented in Figs. 2 and 3 show a good agreement between numerical solutions using the full resistive coefficients and Lie bracket calculation which were based on the quadratic approximation (9), hence we expect the local controllability result to hold for the full coefficients (6).

To verify the theoretical effects of modifying the ratio λ between the length of the central link and that of the outer links, we numerically solve the control system using the full form of the drag coefficients. As shown in Fig. 4 for $\mathbf{h}_t^3$, the numerical results agree closely with the theoretical prediction based on (14). We note that from the x-component of $\mathbf{h}_t^3(\lambda)$, it can be determined that the maximum displacement is obtained at $\lambda = (\sqrt{97} - 1)/8 \approx 1.10611$. We also show the dependence on λ for the vector field $\mathbf{h}_t^4$ in (15) and illustrate the numerical results in Fig. 5. The x-component of $\mathbf{h}_t^4(\lambda)$ is found to be maximized at $\lambda \approx 0.55467$.

 https://doi.org/10.1007/s11012-026-02136-0





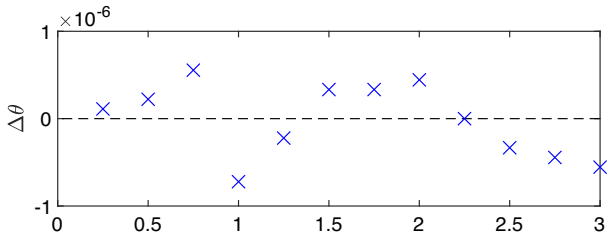
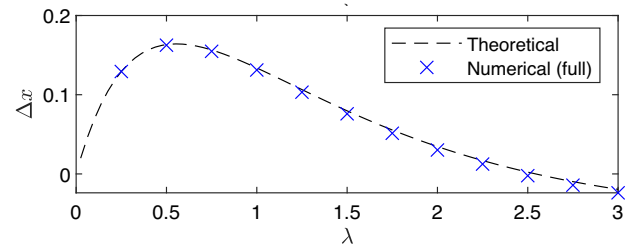
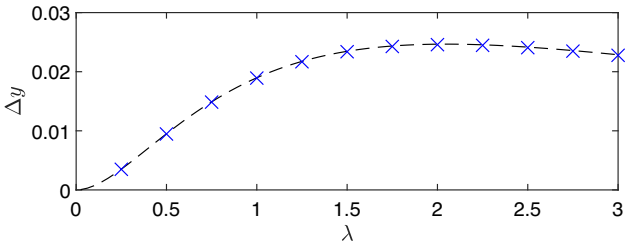


Fig. 4 Comparisons between numerically computed and theoretical displacements Δx, Δy, and $\Delta\theta$ as functions of the link length ratio λ for controls corresponding to the vector field $\mathbf{h}_t^3$ with amplitude $\xi = 10^{-4.5}$. The initial state is $(x_0, y_0, \theta_0, \alpha_0^{(-1)}, \alpha_0^{(1)}) = (0, 10^{-2}, 0, 0, 0)$. The common geometrical parameters used are $L = 1$ and $r = 10^{-4}$. The full drag coefficients (6) are used for the numerical computations





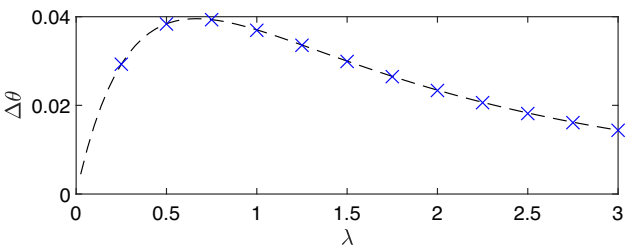


Fig. 5 Comparisons between numerically computed and theoretical displacements Δx, Δy, and $\Delta\theta$ as functions of the link length ratio λ for controls corresponding to the vector field $\mathbf{h}_t^4$ with amplitude $\xi = 10^{-3.5}$. The initial state is $(x_0, y_0, \theta_0, \alpha_0^{(-1)}, \alpha_0^{(1)}) = (0, 10^{-2}, 0, 0, 0)$. The common geometrical parameters used are $L = 1$ and $r = 10^{-4}$. The full drag coefficients (6) are used for the numerical computations

Whereas we only computed the vector fields analytically for the parallel configuration, $\theta_0 = 0$, we show the numerical results for displacements using the piecewise constant controls for $\mathbf{h}_t^3$ starting from slightly tilted swimmer configurations in Fig. 6, recalling that the range of admissible tilt angles is restricted by condition (2). In free space, it is known that the $\mathbf{h}_t^3$ vector field is used to propel the swimmer along its axis while $\mathbf{h}_t^4$ and $\mathbf{h}_t^5$ are used to generate perpendicular and rotational motion. Hence, we decompose the displacement into a component parallel to the tilted axis, a component perpendicular to the axis, and an angular component. The parallel component $|\Delta_\parallel|$ appears to have a local maximum at $\theta_0 \approx 0$, however, we note that the variations in $|\Delta_\parallel|$ with θ_0 are comparable

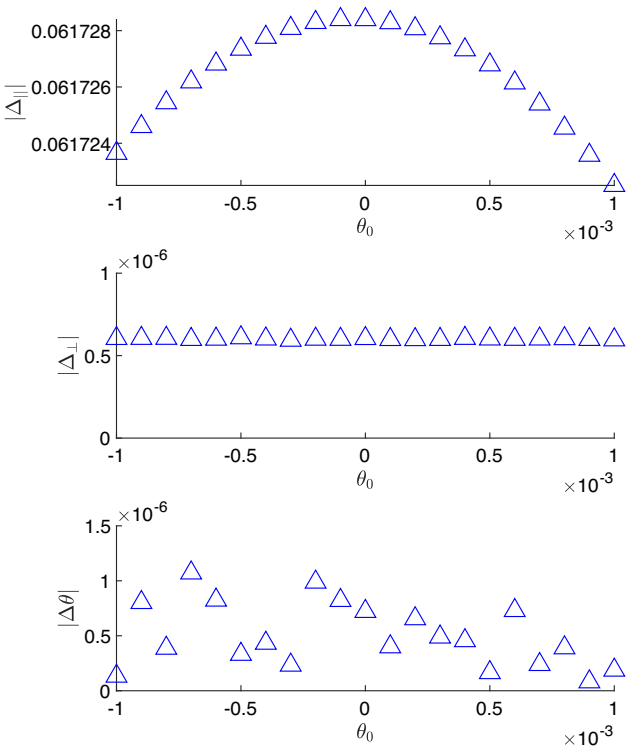


Fig. 6 Numerically computed displacements $|\Delta_\parallel|$, $|\Delta_\perp|$, and $|\Delta\theta|$ in the swimmer parallel, perpendicular, and angular directions as functions of the tilt angle θ_0 with respect to the wall for controls corresponding to the vector field $\mathbf{h}_t^3$. The initial state is $(x_0, y_0, \theta_0, \alpha_0^{(-1)}, \alpha_0^{(1)}) = (0, 10^{-2}, \theta_0, 0, 0)$. The geometrical parameters used are $L = 1$, $\lambda = 1$, $r = 10^{-4}$, and the amplitude parameter is $\xi = 10^{-4.5}$. The full drag coefficients (6) are used in these computations

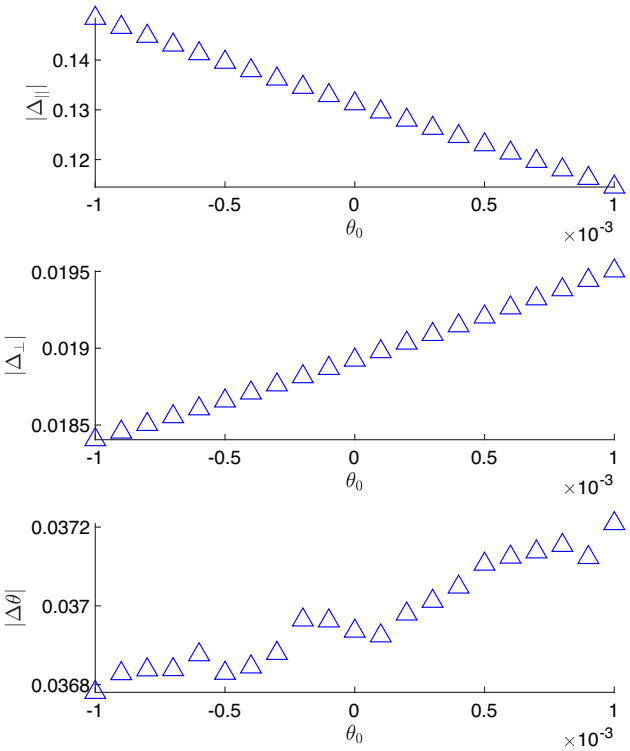


Fig. 7 Numerically computed displacements $|\Delta_\parallel|$, $|\Delta_\perp|$, and $|\Delta\theta|$ in the swimmer parallel, perpendicular, and angular directions as functions of the tilt angle θ_0 with respect to the wall for controls corresponding to the vector field $\mathbf{h}_t^4$. The initial state is $(x_0, y_0, \theta_0, \alpha_0^{(-1)}, \alpha_0^{(1)}) = (0, 10^{-2}, \theta_0, 0, 0)$. The geometrical parameters used are $L = 1$, $\lambda = 1$, $r = 10^{-4}$, and the amplitude parameter is $\xi = 10^{-3.5}$. The full drag coefficients (6) are used in these computations

to the finite-ξ effects shown in Fig. 2. The perpendicular and angular displacements are negligible, showing that even with the wall, the $\mathbf{h}_t^3$ vector field only produces net motion along the axis of the swimmer.

Corresponding analysis of the second-order control in tilted initial configurations is shown in Fig. 7. We find that the parallel displacement decreases approximately linearly and the perpendicular and angular displacements increase approximately linearly with the tilting angle.

5 Conclusions

In this work we have investigated the dynamics and controllability of a Purcell three-link swimmer moving through a viscous fluid in a plane perpendicular to a rigid wall. Starting from a wall-corrected resistive-force theory model, we derived an explicit control system valid for configurations that are nearly parallel to the boundary. Using tools from Geometric Control Theory, previous studies proved that the Purcell swimmer is locally controllable in a free-space domain. We now show that the swimmer remains locally controllable in the presence of a no-slip plane wall when it is nearly parallel to the wall, thereby determining that the wall does not hinder controllability. In fact, the wall's presence has a symmetry-breaking effect and provides a richer structure of the Lie algebra generated by the control vector fields.

All our theoretical predictions are in good agreement with numerical simulations. In particular, we observe that, even though our computation of the brackets $\mathbf{h}_t^i$ $(i = 1, \ldots, 5)$ is done using the approximates drag coefficients of the resistive-force theory (see (9)), the theoretical results so obtained are in good agreement with the numerical simulations performed using the completely nonlinear drag coefficients, as Figs. 2–6 show.

Several directions for future research naturally emerge from our analysis. Our treatment of wall effects based on resistive-force theory is a simplification and limited to asymptotic regimes in which $r \ll y_t \ll L_i$ $(i \in \{\pm 1, 0\})$. Resistance coefficients valid in other regimes have been proposed (such as $y_t \gg L_i$ and for arbitrary ratios of y_t/L_i ; see [18, 20]). Controllability results could be extended to such regimes by considering more general ratios of the normal and tangential drag coefficients. Retaining higher-order terms in expansion (9a) could also allow one to quantify more precisely the range of validity of the present model.

To overcome the limitations of resistive-force theory, particularly near a wall or in other domain geometries, the swimming trajectories can be computed more accurately using numerical methods such as boundary element methods [12, 28] and regularized Stokeslet segments [19, 29]. Such frameworks would enable higher fidelity simulations for practical applications, though their utility in theoretical proofs may be limited.

Allowing more general three-dimensional motion of the swimmer, several qualitatively new phenomena are expected. First, the configuration space becomes higher-dimensional, with additional orientation degrees of freedom, and the presence of a planar wall breaks rotational symmetry in a non-trivial way. A 3D Purcell-type swimmer near a no-slip boundary could exhibit out-of-plane reorientation, circular trajectories, or stable limit cycles analogous to those observed for helical bacteria near surfaces. From a control perspective, it would be natural to investigate whether controllability persists near configurations parallel to the wall and how the Lie algebra structure is modified by the additional rotational degrees of freedom.

Acknowledgements MM is a member of INdAM-GNAMPA; MZ is a member of INdAM-GNFM. EM acknowledges support from the *Master Early Research Honors School* of Politecnico di Torino.

Author Contributions All authors contributed equally.

Funding Open access funding provided by Politecnico di Torino within the CRUI-CARE Agreement. HS acknowledges the support of the Natural Sciences and Engineering Research Council of Canada (NSERC), [funding reference no. RGPIN-2018-04418]. Cette recherche a été financée par le Conseil de recherches en sciences naturelles et en génie du Canada (CRSNG), [numéro de référence RGPIN-2018-04418]. MM and MZ acknowledge funding from the *Mathematics for Industry 4.0* 2020F3NCPX PRIN2020, funded by the Italian MUR. MZ received funding from the INdAM - GNFM Project *Modeling and control of electrically actuated slender microswimmers* [CUP E53240019500001].

Data Availability No datasets were generated or analysed during the current study.

Code Availability Not applicable.

Declarations

Conflicts of Interest The authors declare no conflict of interest.

Ethical Approval and Consent to Participate Not applicable.

Consent for Publication Not applicable.

Open Access This article is licensed under a Creative Commons Attribution 4.0 International License, which permits use, sharing, adaptation, distribution and reproduction in any medium or format, as long as you give appropriate credit to the original author(s) and the source, provide a link to the Creative Commons licence, and indicate if changes were made. The images or other third party material in this article are included in the article's Creative Commons licence, unless indicated otherwise in a credit line to the material. If material is not included in the article's Creative Commons licence and your intended use is not permitted by statutory regulation or exceeds the permitted use, you will need to obtain permission directly from the copyright holder. To view a copy of this licence, visit http://creativecommons.org/licenses/by/4.0/.

References

1. Purcell EM (1977) Life at low Reynolds number. Am J Phys 45:3–11. https://doi.org/10.1119/1.10903
2. Becker LE, Koehler SA, Stone HA (2003) On self-propulsion of micro-machines at low Reynolds number: Purcell's three-link swimmer. J Fluid Mech 490:15–35. https://doi.org/10.1017/S0022112003005184
3. Giraldi L, Martinon P, Zoppello M (2013) Controllability and Optimal Strokes for *N*-link Microswimmer. In: 52nd IEEE Conference on Decision and Control
4. Kadam S, Banavar RN (2016) Geometric controllability of the Purcell's swimmer and its symmetrized cousin. IFAC-PapersOnLine 49(18):988–993. https://doi.org/10.1016/j.ifacol.2016.10.296
5. Marchello R, Morandotti M, Shum H, Zoppello M (2022) The *N*-link swimmer in three dimensions: controllability and optimality results. Acta Appl Math 178:6–25. https://doi.org/10.1007/s10440-022-00480-3
6. Giraldi L, Martinon P, Zoppello M (2015) Optimal design of Purcell's three-link swimmer. Phys Rev E 91:023012. https://doi.org/10.1103/PhysRevE.91.023012
7. Wiezel O, Or Y (2016) Optimization and small-amplitude analysis of Purcell's three-link microswimmer model. Proceedings of the Royal Society A Mathematical Physical and Engineering Sciences 472(2192):20160425. https://doi.org/10.1098/rspa.2016.0425
8. Berke AP, Turner L, Berg HC, Lauga E (2008) Hydrodynamic Attraction of Swimming Microorganisms by Surfaces. Phys Rev Lett 101(3):038102. https://doi.org/10.1103/PhysRevLett.101.038102
9. Frymier PD, Ford RM, Berg HC, Cummings PT (1995) Three-dimensional tracking of motile bacteria near a solid planar surface. Proc Natl Acad Sci 92(13):6195–6199. https://doi.org/10.1073/pnas.92.13.619
10. Lauga E, DiLuzio WR, Whitesides GM, Stone HA (2006) Swimming in circles: Motion of bacteria near solid boundaries. Biophys J 90(2):400–412. https://doi.org/10.1529/biophysj.105.069401
11. Rothschild (1963) Non-random Distribution of Bull Spermatozoa in a Drop of Sperm Suspension. Nature 198(4886), 1221–1222 https://doi.org/10.1038/1981221a0. Number: 4886 Publisher: Nature Publishing Group
12. Shum H, Gaffney EA, Smith DJ (2010) Modelling bacterial behaviour close to a no-slip plane boundary: the influence of bacterial geometry. Proceedings of the Royal Society A 466(2118):1725–1748. https://doi.org/10.1098/rspa.2009.0520
13. Ishimoto K, Gaffney EA (2014) A study of spermatozoan swimming stability near a surface. J Theor Biol 360:187–199. https://doi.org/10.1016/j.jtbi.2014.06.034
14. Spagnolie SE, Lauga E (2012) Hydrodynamics of self-propulsion near a boundary: predictions and accuracy of far-field approximations. J Fluid Mech 700:105–147. https://doi.org/10.1017/jfm.2012.101
15. Gray J, Hancock GJ (1955) The Propulsion of Sea-Urchin Spermatozoa. J Exp Biol 32(4):802–814. https://doi.org/10.1242/jeb.32.4.802
16. Keller JB, Rubinow SI (1976) Slender-body theory for slow viscous flow. J Fluid Mech 75(4):705–714. https://doi.org/10.1017/S0022112076000475
17. Johnson RE, Brokaw CJ (1979) Flagellar hydrodynamics. a comparison between resistive-force theory and slender-body theory. Biophys J 25(1):113–127. https://doi.org/10.1016/S0006-3495(79)85281-9
18. Katz DF, Blake JR, Paveri-Fontana SL (1975) On the movement of slender bodies near plane boundaries at low Reynolds number. J Fluid Mech 72(3):529–540. https://doi.org/10.1017/S0022112075003126
19. Walker BJ, Ishimoto K, Gadêlha H, Gaffney EA (2019) Filament mechanics in a half-space via regularised Stokeslet segments. J Fluid Mech 879:808–833. https://doi.org/10.1017/jfm.2019.723

20. Koens L, Montenegro-Johnson TD (2021) Local drag of a slender rod parallel to a plane wall in a viscous fluid. Phys Rev Fluids 6:064101. https://doi.org/10.1103/PhysRevFluids.6.064101
21. Teng J, Rallabandi B, Stone HA, Ault JT (2022) Coupling of translation and rotation in the motion of finite-length rods near solid boundaries. J Fluid Mech 938:30. https://doi.org/10.1017/jfm.2022.177
22. Długosz M, Cichocki B, Szymczak P (2022) Estimating near-wall diffusion coefficients of arbitrarily shaped rigid macromolecules. Phys Rev E 106:014407. https://doi.org/10.1103/PhysRevE.106.014407
23. Jakuszeit T, Croze OA (2024) Role of tumbling in bacterial scattering at convex obstacles. Phys Rev E 109:044405. https://doi.org/10.1103/PhysRevE.109.044405
24. Smith DJ, Gaffney EA, Blake JR, Kirkman-Brown JC (2009) Human sperm accumulation near surfaces: a simulation study. J Fluid Mech 621:289–320. https://doi.org/10.1017/S0022112008004953
25. Brennen C, Winet H (1977) Fluid mechanics of propulsion by cilia and flagella. Annu Rev Fluid Mech9:339–398. https://doi.org/10.1146/annurev.fl.09.010177.002011
26. Agrachev AA, Sachkov YL (2004) Control Theory from the Geometric Viewpoint. Springer, Berlin Heidelberg
27. Coron J-M (2007) Control and Nonlinearity. Mathematical Suveys and Monographs, vol. 1. Am. Math. Soc., Providence, RI
28. Ramia M, Tullock DL, Phan-Thien N (1993) The role of hydrodynamic interaction in the locomotion of microorganisms. Biophys J 65(2):755–778. https://doi.org/10.1016/S0006-3495(93)81129-9
29. Cortez R (2018) Regularized Stokeslet segments. J Comput Phys 375:783–796. https://doi.org/10.1016/j.jcp.2018.08.055

Authors and Affiliations

Enrico Micalizio[1] · Marco Morandotti[1] · Henry Shum[2] · Marta Zoppello[1]

✉ Marta Zoppello
marta.zoppello@polito.it

Enrico Micalizio
enrico.micalizio@studenti.polito.it

Marco Morandotti
marco.morandotti@polito.it

Henry Shum
henry.shum@uwaterloo.ca

[1] Department of Mathematical Sciences, Politecnico di Torino, Corso Duca degli Abruzzi, 24, Torino 10129, Italy

[2] Department of Applied Mathematics and Waterloo Institute forNanotechnology, University of Waterloo, Waterloo ON N2L 3G1 , Canada